THE ARCHIVE OF MECHANICAL ENGINEERING

VOL. LX 2013 Number 3

10.2478/meceng-2013-0027

Key words: finite element methods, vibration analysis, experimental verification

IWONA ADAMIEC-WÓJCIK [*], *ANDRZEJ NOWAK* [**], *STANISŁAW WOJCIECH* [***]

COMPARISON OF METHODS FOR MODELLING VIBRATIONS OF COLLECTING ELECTRODES IN DRY ELECTROSTATIC PRECIPITATORS

Dry electrostatic precipitators (ESPs) are widely used for purification of exhaust gases in industrial applications. Maintenance of their high efficiency depends primarily on periodical cleaning of the collecting electrodes (CEs). Dust removal (regeneration of CEs) is realized by inducing periodical vibrations of the electrodes. The paper presents results of vibration modelling of a system of CEs; the results were obtained by means of the finite element method, the hybrid finite element method, the finite strip method and a model formulated using Abaqus. Numerical results are compared with those obtained from experimental measurements. Conclusions concerning numerical effectiveness and exactness of the methods are formulated and reasons for differences are discussed.

1. Introduction

Contamination of the atmosphere by polydisperse dust emitted together with waste gases from electrical and industrial plants has been a source of serious health and ecological problems for many years [1-3]. Dry electrostatic precipitators (ESP) are widely used for purification of exhaust gases in industrial applications.

The inside of an ESP is a complex steel construction containing many sections (Fig. 1a). One section is formed by up to one hundred systems of collecting electrodes separated alternately by systems of discharge electrodes (Fig. 1b). Effectiveness of an ESP depends on conditions of gas flow, electri-

[*] *University of Bielsko-Biała, ul. Willowa 2, 43-309 Bielsko-Biała, Email: i.adamiec@ath.eu*

[**] *University of Bielsko-Biała, ul. Willowa 2, 43-309 Bielsko-Biała, Email: a.nowak@ath.eu*

[***] *University of Bielsko-Biała, ul. Willowa 2, 43-309 Bielsko-Biała, Email: swojciech@ath.eu*

cal field, and geometrical parameters of the collecting electrodes. Evaluation of the precipitator efficiency is realized either directly by measurements or indirectly by the use of physical laboratory models or computer simulations based on mathematical models.

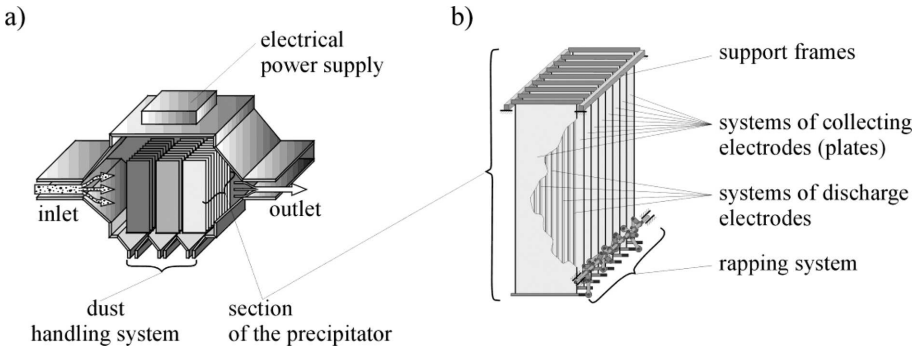

Fig. 1. Dry electrostatic precipitator: a) scheme of an ESP, b) section of the precipitator

Recently a great deal of research has been devoted to measuring and modelling the electrical field [4-7] and gas flow in ESPs [5], [8]. Mechanical phenomena, especially vibrations induced during the process of cleaning the electrodes, are rarely analysed [2], [9]. Regardless of the type of the device used for shaking off the dust (gravitational, electro-vibrational, acoustic), cleaning of the collecting electrodes is realized by inducing vibrations, the propagation of which in the system of CEs causes coagulated dust particles to be detached and thereby removed from the precipitator. Geometrical parameters of CEs and the impulse force generating the vibrations in the system have a direct impact on normal and tangent accelerations of CEs, and thus on the effectiveness of the regeneration process. On the one hand, the range of the accelerations obtained influences the effectiveness of the cleaning process, but on the other hand it determines the values of fatigue load. A reasonable compromise requires modern calculation methods to be used at the design stage.

The authors have, for several years, dealt with the modelling and measurement of the vibrations of the electrodes caused by the beater hitting the brushing bar. Paper [10] presents the results of research devoted to optimisation of the shape of the beater. This paper is concerned with modelling of one system of the collecting electrodes (Fig. 2a), which consists of the suspension beam (upper beam) and the set of p hanging electrodes (usually no more than 10) braced at the bottom by the brushing bar (bottom beam).

The beater hits an anvil placed at the end of the brushing bar. The vibrations are induced by force $F(t)$, the exemplary course of which (measured at the test stand) is presented in Fig. 2c). A collecting electrode (CE) consists

of several long strips connected at certain angles. The test stand, where the measurements were taken, was equipped with SIGMA VI electrodes (Fig. 2b) and such electrodes are considered in this paper.

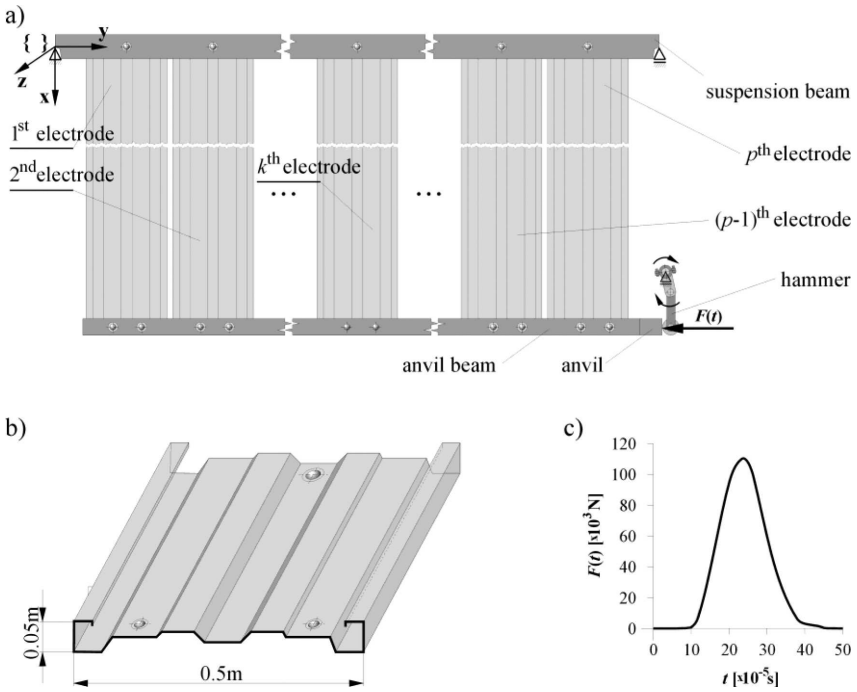

Fig. 2. The system under consideration: a) the system of collecting electrodes, b) SIGMA VI profile, c) measured impulse force

Different modelling methods are applied. The model obtained by means of the finite element method is presented in [11] and [12]. The model based on the hybrid finite element method (HFEM) combining the rigid finite element method with the finite element method (FEM) is presented in [13], while paper [14] describes the model formulated using the finite strip method (FSM). The hybrid finite element method and the finite strip method are also presented in [15] together with the analysis of free vibrations. Forced vibrations were not considered there.

This paper presents, for the first time, comparison of all the above methods with respect to their exactness and effectiveness in analysis of vibrations forced by the hammer. The description of the methods is limited to a minimum; only the basic features are shown, omitting transformations and relations which can be found in the papers mentioned above. The results of calculations carried out according to our own methods are compared with those obtained using Abaqus and from experimental measurements.

2. Models of the system

The mathematical model takes into account:
- the upper beam simply supported,
- p electrodes, which are shells connected with the upper beam; the electrode can rotate about an axis parallel to $\mathbf{z}$,
- the bottom beam rigidly connected with the electrodes and loaded with the impulse force as in Fig. 2c.

Damping is omitted in the models. The models of beams are obtained using the rigid finite element method [16], according to which the beams are divided into n_u and n_d massless and non-dimensional elements respectively as in Fig. 3.

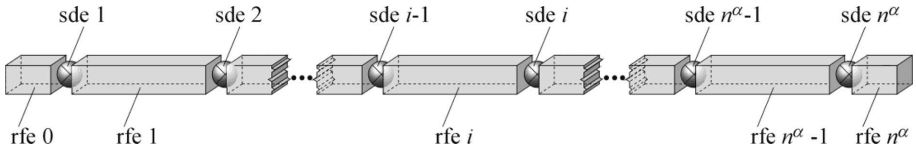

Fig. 3. Discretisation of beam α ($\alpha \in \{u, d\}$) into rigid (rfe) and spring-damping (sde) elements

Equations of motion of the beams can be written in the following form:

$$\mathbf{M}^{(\alpha)}\ddot{\mathbf{q}}^{(\alpha)} + \mathbf{C}^{(\alpha)}\mathbf{q}^{(\alpha)} = \mathbf{G}^{(\alpha)} + \mathbf{Q}^{(\alpha)} \tag{1}$$

where: $\mathbf{q}^{(\alpha)} = \left[\begin{array}{ccccc} \mathbf{q}_0^{(\alpha)\mathrm{T}} & \cdots & \mathbf{q}_i^{(\alpha)\mathrm{T}} & \cdots & \mathbf{q}_{n^\alpha}^{(\alpha)\mathrm{T}} \end{array} \right]^{\mathrm{T}}$,

$\mathbf{q}_i^{(\alpha)} = \left[\begin{array}{cccccc} x_i^\alpha & y_i^\alpha & z_i^\alpha & \varphi_i^\alpha & \theta_i^\alpha & \psi_i^\alpha \end{array} \right]^{\mathrm{T}}$,

$x_i^\alpha, y_i^\alpha, z_i^\alpha$ – translational displacements of the centre of mass of the rfe,

$\varphi_i^\alpha, \theta_i^\alpha, \psi_i^\alpha$ – rotational displacements of the rfe,

$\mathbf{M}^{(\alpha)}$ – diagonal matrices with constant coefficients,

$\mathbf{C}^{(\alpha)}$ – stiffness matrices with constant coefficients,

$\mathbf{G}^{(\alpha)}$ – vector of gravity forces,

$\mathbf{Q}^{(\alpha)}$ – vector of external generalised forces caused by the impulse force presented in Fig. 2 acting on the bottom beam.

The electrodes treated as shells with large length (about 20 meters) are modelled using three different methods:
- classical finite element method (FEM)
- hybrid finite element method, which combines the finite element method with the rigid finite element method (HFEM)
- finite strip method (FSM).

The most important elements of the model are described in the next subsections.

2.1. FEM model

The system of coordinates $\{k\}$ with axes as in Fig. 4 is assigned to electrode k. A single strip of the electrode has constant width and thickness. Each strip is divided into n_k elements with constant length Δx_k along axis $\hat{\mathbf{x}}$.

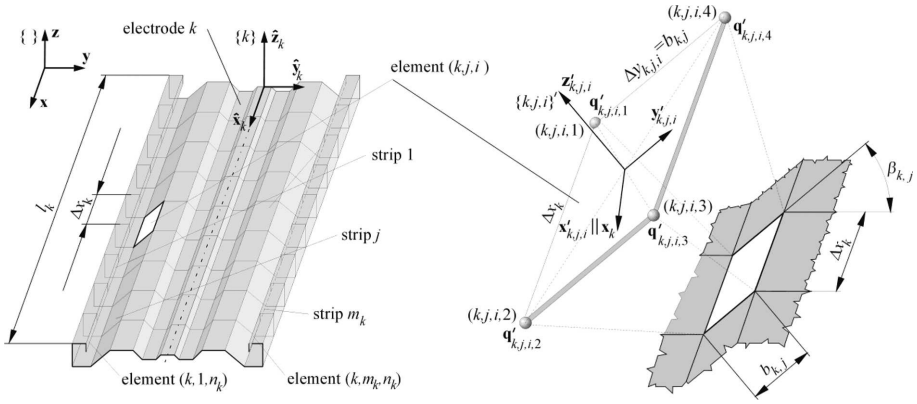

Fig. 4. Strip j with width $b_{k,j}$ and angle of inclination $\beta_{k,j}$ towards axis $\hat{\mathbf{y}}$, {} – global coordinate system, $\{k\}$ – local coordinate system connected with electrode k with axes parallel to those of system {}

Rectangular element (k, j, i) presented in Fig. 4 (indices k, j, i are the numbers of electrode, strip and element in strip j respectively) is described by the following vectors:

$$\mathbf{q}'_{k,j,i,s} = \left[u'_{k,j,i,s}, v'_{k,j,i,s}, w'_{k,j,i,s}, \varphi'_{k,j,i,s}, \theta'_{k,j,i,s}, \psi'_{k,j,i,s}\right]^{\mathrm{T}} \text{ for } s = 1,2,3,4 \tag{2}$$

where: $u'_{k,j,i,s}$, $v'_{k,j,i,s}$, $w'_{k,j,i,s}$ – displacements of node (k, j, i, s) along axes $\mathbf{x}'_{k,j,i}$, $\mathbf{y}'_{k,j,i}$, $\mathbf{z}'_{k,j,i}$,

$\varphi'_{k,j,i,s}, \theta'_{k,j,i,s}, \psi'_{k,j,i,s}$ – rotations in joint (k, j, i, s) about the axis parallel to $\mathbf{x}'_{k,j,i}$, $\mathbf{y}'_{k,j,i}$, $\mathbf{z}'_{k,j,i}$ respectively.

It is assumed that the shield state is defined by displacements and rotation angle. Displacement fields u', v' are described by the following functions:

$$u'(x', y', t) = a_1^u + a_2^u x' + a_3^u y' + a_4^u x'y' + a_5^u (y')^2 + a_6^u x'(y')^2 \tag{3.1}$$

$$v'(x', y', t) = a_1^v + a_2^v x' + a_3^v y' + a_4^v x'y' + a_5^v (x')^2 + a_6^v (x')^2 y' \tag{3.2}$$

while angles of rotation ψ' are expressed by the relations [17]:

$$\psi' = \frac{1}{2}\left(-\frac{\partial u'}{\partial y'} + \frac{\partial v'}{\partial x'}\right). \tag{3.3}$$

The plate state is described by deflection and angles and defined as follows:

$$w'(x', y', t) = a_1^{(w)} + a_2^{(w)}x' + a_3^{(w)}y' + a_4^{(w)}(x')^2 + a_5^{(w)}x'y' + a_6^{(w)}(y')^2 + \\ + a_7^{(w)}(x')^3 + a_8^{(w)}(x')^2y' + a_9^{(w)}x'(y')^2 + a_{10}^{(w)}(y')^3 + a_{11}^{(w)}(x')^3y' + a_{12}^{(w)}x'(y')^3, \tag{4.1}$$

$$\varphi' = \frac{\partial w'}{\partial y'}, \tag{4.2}$$

$$\theta' = -\frac{\partial w'}{\partial x'}. \tag{4.3}$$

Coefficients $a_1^{(u)} - a_6^{(u)}$, $a_1^{(v)} - a_6^{(v)}$ and $a_1^{(w)} - a_{12}^{(w)}$ can be calculated from the respective boundary conditions dependent on joint displacements and velocities [11], [15].

After necessary transformations presented in [11], the kinetic and potential energy are written as:

$$T_{k,j,i} = \frac{1}{2}\sum_{l=1}^{4}\sum_{s=1}^{4}\dot{q}_{k,j,i,l}^{\mathrm{T}}\mathbf{M}_{k,j,i,l}\dot{q}_{k,j,i,s} \tag{5}$$

$$E_{k,j,i} = \frac{1}{2}\sum_{l=1}^{4}\sum_{s=1}^{4}q_{k,j,i,l}^{\mathrm{T}}\mathbf{C}_{k,j,i,l}q_{k,j,i,s} \tag{6}$$

where: $\mathbf{M}_{k,j,i,l}$, $\mathbf{C}_{k,j,i,l}$ – mass and stiffness matrices of elements expressed with respect to the coordinate system,

$\mathbf{q}_{k,j,i,s} = \mathbf{R}_{k,j}\mathbf{q'}_{k,j,i,s}$ – vectors of nodal displacements expressed with respect to the global coordinate system $\{k, j, i\}$,

$$\mathbf{R}_{k,j} = \begin{bmatrix} \bar{\mathbf{R}}_{k,j} & 0 \\ 0 & \bar{\mathbf{R}}_{k,j} \end{bmatrix},$$

$$\bar{\mathbf{R}}_{k,j} = \begin{bmatrix} 1 & 0 & 0 \\ 0 & \cos\beta_{k,j} & -\sin\beta_{k,j} \\ 0 & \sin\beta_{k,j} & \cos\beta_{k,j} \end{bmatrix}.$$

Finally, after some transformations [11],[12], equations of motion of electrode k can be written in the form:

$$\mathbf{M}_F^{(k)}\ddot{\mathbf{q}}_F^{(k)} + \mathbf{C}_F^{(k)}\mathbf{q}_F^{(k)} = \mathbf{G}_F^{(k)} \tag{7}$$

where: $\mathbf{M}_F^{(k)}$, $\mathbf{C}_F^{(k)}$ – mass and stiffness matrices of electrode k with constant elements,

$$\mathbf{G}_F^{(k)} = -\frac{\partial V_g^{(k)}}{\partial \mathbf{q}_F^{(k)}} - \text{vector of gravity forces,}$$

$$\mathbf{q}_F^{(k)} = \begin{bmatrix} \mathbf{q}_{F,1}^{(k)} \\ \vdots \\ \mathbf{q}_{F,i}^{(k)} \\ \vdots \\ \mathbf{q}_{F,n_F^{(k)}}^{(k)} \end{bmatrix},$$

$\mathbf{q}_{F,n_F^{(k)}}^{(k)}$ – vector of nodal displacements,

$n_F^{(k)} = (n_k + 1)(m_k + 1)$.

The number of generalised coordinates of electrode k is $6n_F^{(k)}$.

2.2. HFEM model

Discretisation of the electrode in the hybrid element method is carried out in two steps. First, the primary division of each strip of the electrode $\left(j = 1, \ldots, n_y\right)$ into finite shell, four-node, rectangular elements (fes) is performed as in the method presented in section 2.1. This stage enables us to calculate the energy of spring deformation. During the next step of discretisation, in accordance with the idea of the rigid finite element method, the body considered is divided into the rigid finite elements (rfes) which assume inertial features (Fig. 5).

Displacements and rotations of the rfe about its main inertial axes (Fig. 6) are the generalised coordinates of the rfe:

$$\mathbf{q}'_{k,l} = \left[\begin{array}{cccccc} \Delta x'_{k,l} & \Delta y'_{k,l} & \Delta z'_{k,l} & \Delta\varphi' & \Delta\theta'_{k,l} & \Delta\psi'_{k,l} \end{array} \right]. \tag{8}$$

Mass matrix of rfe l is diagonal, has constant elements and can be written in the form:

$$\mathbf{M}_{k,l} = diag\left\{ \begin{array}{cccccc} m_{k,l} & m_{k,l} & m_{k,l} & I_{k,l}^x & I_{k,l}^y & I_{k,l}^z \end{array} \right\}, \tag{9}$$

where: $m_{k,l}$ – mass of rfe l,

$I_{k,l}^x, I_{k,l}^y, I_{k,l}^z$ – mass moments of inertia of rfe l,

and since the generalised coordinates of the rfe are independent, the mass matrix of the system of $n_H^{(k)}$ elements takes the following form:

$$\mathbf{M}_H^{(k)} = diag\left\{ \begin{array}{cccc} \mathbf{M}_{k,1} & \mathbf{M}_{k,2} & \cdots & \mathbf{M}_{k,n_H^{(k)}} \end{array} \right\} \tag{10}$$

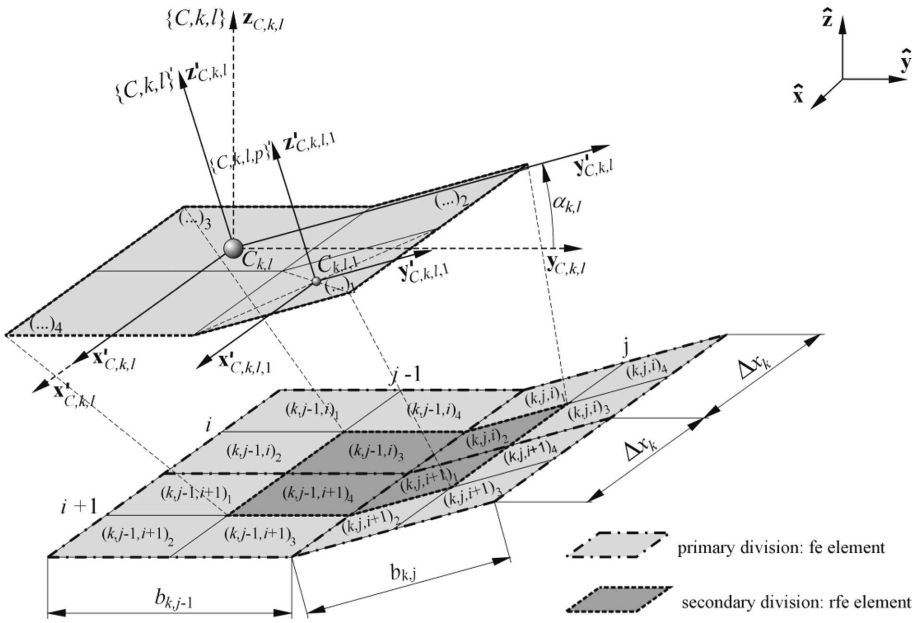

Fig. 5. Discretisation: primary and secondary divisions

Displacements of rfes cause deformations of primary elements. The algorithm enabling the transformation of coordinates of rfes into the elastic coordinates of primary elements and thus formulation of stiffness matrix $\mathbf{C}^{(k)}$ of electrode k is presented in [13] and [11].

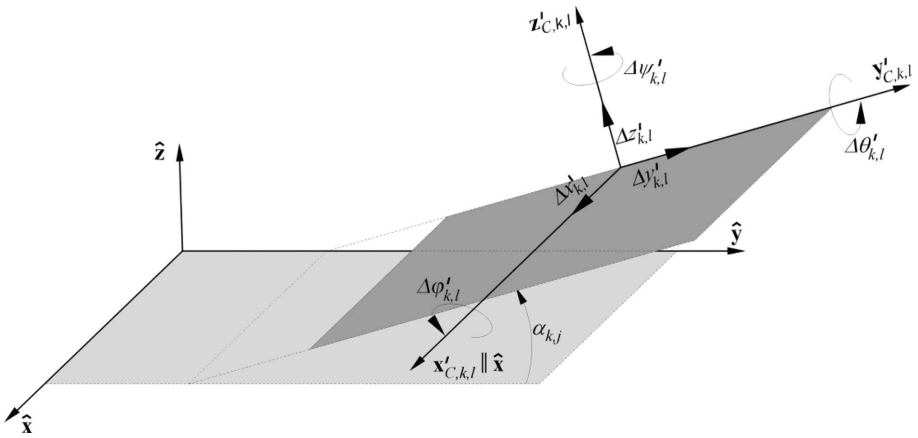

Fig. 6. Generalised coordinates of rfe l

The equations of motion of electrode k can be written in the same form as for the FEM model:

$$\mathbf{M}_H^{(k)}\ddot{\mathbf{q}}_H^{(k)} + \mathbf{C}_H^{(k)}\mathbf{q}_H^{(k)} = \mathbf{G}_H^{(k)} \tag{11}$$

where: $\mathbf{M}_H^{(k)}$ – mass matrix,

$\mathbf{C}_H^{(k)}$ – stiffness matrix with constant elements,

$\mathbf{G}_h^{(k)} = -\dfrac{\partial V_g^{(k)}}{\partial \mathbf{q}_H^{(k)}}$ – vector of gravity forces,

$$\mathbf{q}_H^{(k)} = \begin{bmatrix} \mathbf{q'}_{k,1} \\ \vdots \\ \mathbf{q'}_{k,l} \\ \vdots \\ \mathbf{q}_{k,n_H^{(k)}} \end{bmatrix},$$

$\mathbf{q'}_{k,l}$ – defined in (8),

$n_H^{(k)} = (n_k + 1)(m_k + 1)$.

As in the FEM model the number of generalised coordinates is also $n_H^{(k)}$, but the interpretation of coordinates is different.

2.3. FSM model

In the case of the finite strip method it is assumed that the field of displacements of strip j of electrode k is described by the following functions:

$$u'(x', y', t) = X(x', t)\, Y_{k,j}^{(u)}(y'), \tag{12.1}$$

$$v'(x', y', t) = X(x', t)\, Y_{k,j}^{(v)}(y'), \tag{12.2}$$

$$w'(x', y', t) = X(x', t)\, Y_{k,j}^{(w)}(y'), \tag{12.3}$$

where: – coordinates as in Fig. 7,

$X(x', t) = \sum_{i=-1}^{n_k+1} a_i(t)\, \phi_i(x')$,

$(n_k + 3)$ – number of terms in the approximation series $X(x', t)$,

$Y_{k,j}^{(u)} = \mathbf{P}_{k,j}(y')\, \mathbf{q'}_{k,j}^{(u)}, \quad Y_{k,j}^{(v)} = \mathbf{P}_{k,j}(y')\, \mathbf{q'}_{k,j}^{(v)}, \quad Y_{k,j}^{(w)} = \mathbf{P}_{k,j}(y')\, \mathbf{q'}_{k,j}^{(w)}$,

$$\mathbf{P}_{k,j}(y') = \left[-\frac{y'}{b_{k,j}} + 1, \quad \frac{y'}{b_{k,j}} \right],$$

$$\mathbf{Q}_{k,j}(y') = \left[1 - \frac{3y'^2}{b_{k,j}^2} + \frac{2y'^3}{b_{k,j}^3}, y' - \frac{2y'^2}{b_{k,j}} + \frac{y'^3}{b_{k,j}^2}, \frac{3y'^2}{b_{k,j}^2} - \frac{2y'^3}{b_{k,j}^3}, -\frac{y'^2}{b_{k,j}} - \frac{y'^3}{b_{k,j}^2} \right],$$

$$\mathbf{q}'^{(u)}_{k,j} = \begin{bmatrix} u'_{k,j,1} \\ u'_{k,j,2} \end{bmatrix}, \quad \mathbf{q}'^{(v)}_{k,j} = \begin{bmatrix} v'_{k,j,1} \\ v'_{k,j,2} \end{bmatrix}, \quad \mathbf{g}'^{(w)}_{k,j} = \begin{bmatrix} w'_{k,j,1} \\ \varphi'_{k,j,1} \\ w'_{k,j,2} \\ \varphi'_{k,j,2} \end{bmatrix}.$$

The functions $\phi_i(x')$ appearing above are defined as follows [18]:

$$\phi_i(x') = \begin{cases} 0 & x' < x'_{i-2} \\ \left(x' - x'_{i-2}\right)^3 & x'_{i-2} \le x' \le x'_{i-1} \\ h^3 + 3h^2\left(x' - x'_{i-1}\right) + 3h\left(x' - x'_{i-1}\right)^2 - 3\left(x' - x'_{i-1}\right)^3 & x'_{i-1} \le x' \le x'_i \\ h^3 - 3h^2\left(x' - x'_{i+1}\right) + 3h\left(x' - x'_{i+1}\right)^2 + 3\left(x' - x'_{i+1}\right)^3 & x'_i \le x' \le x'_{i+1} \\ \left(x'_{i+2} - x'\right)^3 & x'_{i+1} \le x' \le x'_{i+2} \\ 0 & x'_{i+2} < x' \end{cases} \quad (13)$$

After transformations described in detail in [14], the kinetic and potential energy of strip j of electrode k can be written in the following forms:

$$T_{k,j} = \frac{1}{2} \sum_{i=-1}^{n_k+1} \begin{bmatrix} \dot{\mathbf{q}}^{\mathrm{T}}_{k,j,i,1} & \dot{\mathbf{q}}^{\mathrm{T}}_{k,j,i,2} \end{bmatrix} \sum_{l=-1}^{n_k+1} \begin{bmatrix} \mathbf{M}_{k,j,i,l,1,1} & \mathbf{M}_{k,j,i,l,1,2} \\ \mathbf{M}_{k,j,i,l,2,1} & \mathbf{M}_{k,j,i,l,2,2} \end{bmatrix} \begin{bmatrix} \dot{\mathbf{q}}_{k,j,i,1} \\ \dot{\mathbf{q}}_{k,j,i,2} \end{bmatrix}, \quad (14)$$

$$E_{k,j} = \frac{1}{2} \sum_{i=-1}^{n_k+1} \begin{bmatrix} \mathbf{q}^{\mathrm{T}}_{k,j,i,1} & \mathbf{q}^{\mathrm{T}}_{k,j,i,2} \end{bmatrix} \sum_{l=-1}^{n_k+1} \begin{bmatrix} \mathbf{C}_{k,j,i,l,1,1} & \mathbf{C}_{k,j,i,l,1,2} \\ \mathbf{C}_{k,j,i,l,2,1} & \mathbf{C}_{k,j,i,l,2,2} \end{bmatrix} \begin{bmatrix} \mathbf{q}_{k,j,i,1} \\ \mathbf{q}_{k,j,i,2} \end{bmatrix}, \quad (15)$$

where: $\mathbf{M}_{k,j,i,l,\alpha,\beta}$, $\mathbf{C}_{k,j,i,l,\alpha,\beta}$ – matrices with constant elements,

$$\hat{\mathbf{R}}_{k,j} = \begin{bmatrix} 1 & 0 & 0 & 0 \\ 0 & \cos\beta_{k,j} & -\sin\beta_{k,j} & 0 \\ 0 & \sin\beta_{k,j} & \cos\beta_{k,j} & 0 \\ 0 & 0 & 0 & 1 \end{bmatrix},$$

$$\mathbf{q}'_{k,j,i,s} = \begin{bmatrix} a_i u'_{k,j,s} \\ a_i v'_{k,j,s} \\ a_i w'_{k,j,s} \\ a_i \varphi'_{k,j,s} \end{bmatrix},$$

$$\mathbf{q}_{k,j,i,s} = \hat{\mathbf{R}}_{k,j} \mathbf{q}'_{k,j,i,s}.$$

The vectors of generalised coordinates of the electrodes can be presented as follows:

$$\mathbf{q}_{k,j} = \begin{bmatrix} \mathbf{q}_{k,0,i} \\ \mathbf{q}_{k,1,i} \\ \vdots \\ \mathbf{q}_{k,j,i} \\ \vdots \\ \mathbf{q}_{k,m_k-1,i} \\ \mathbf{q}_{k,m_k,i} \end{bmatrix}, \tag{16}$$

where: $\mathbf{q}_{k,j,i} = \left[u_{k,j,i} v_{k,j,i} w_{k,j,i} \varphi_{k,j,i}\right]^T$ for $j = 0, 1, \ldots, m_k$,
$\mathbf{q}_{k,0,i} = \mathbf{q}_{k,1,i,1}$,
$\mathbf{q}_{k,j,i} = \mathbf{q}_{k,j,i,2} = \mathbf{q}_{k,j+1,i,1}$ for $j = 1, \ldots, m_k - 1$,
$\mathbf{q}_{k,m_k,i} = \mathbf{q}_{k,m_k,2}$.

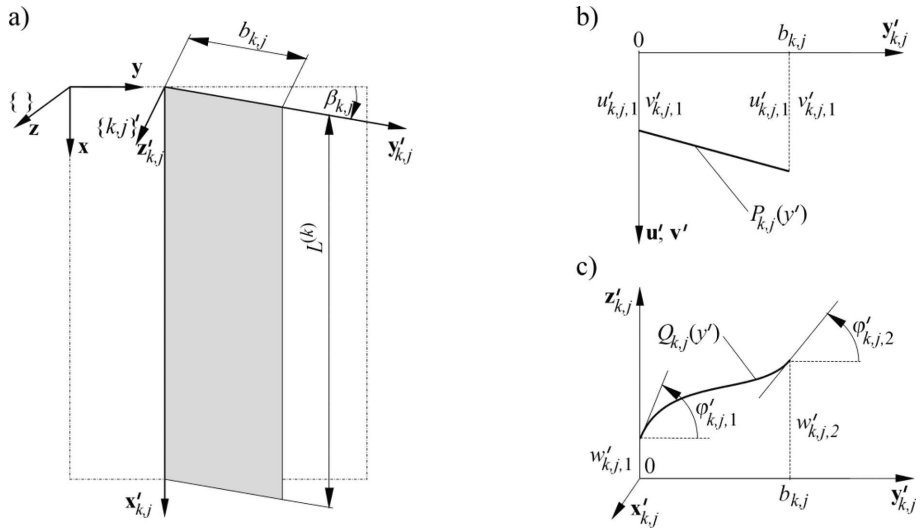

Fig. 7. Models of displacements of strip j of electrode k : a) coordinate system $\{k, j\}'$, b) nodal displacements $u'_{k,j,1}, v'_{k,j,1}, u'_{k,j,2}, v'_{k,j,2}$ – polynomial $\mathbf{P}_{k,j}(y')$, c) nodal displacements $w'_{k,j,1}, \varphi'_{k,j,1}, w'_{k,j,2}, \varphi'_{k,j,2}$– polynomial $\mathbf{Q}_{k,j}(y')$

After some transformations, the equations of motion of the electrode are written as:

$$\mathbf{M}_S^{(k)} \ddot{\mathbf{q}}_S^{(k)} + \mathbf{C}_S^{(k)} \mathbf{q}_S^{(k)} = \mathbf{G}_S^{(k)}, \tag{17}$$

where: $\mathbf{q}_S^{(k)} = \begin{bmatrix} \mathbf{q}_{k,-1} \\ \mathbf{q}_{k,0} \\ \vdots \\ \mathbf{q}_{k,i} \\ \vdots \\ \mathbf{q}_{k,n_k} \\ \mathbf{q}_{k,n_k+1} \end{bmatrix}$,

$\mathbf{M}_S^{(k)}$, $\mathbf{C}_S^{(k)}$ – matrices with constant elements,

$\mathbf{G}_S^{(k)} = -\dfrac{\partial V_g^{(k)}}{\partial \mathbf{q}_S^{(k)}}$ – vector of gravity forces.

The number of generalised coordinates describing the motion of the electrode k is $4\,(n_k + 3)\,(m_k + 1)$.

2.4. Connection between beams and electrodes

Because elastic connections are introduced between the beams and the electrodes, there appear the coupling between vectors $\mathbf{q}^{(u)}$ and $\mathbf{q}^{(k)}$ as well as vectors $\mathbf{q}^{(k)}$ and $\mathbf{q}^{(d)}$. In our research we assume that the connections between the beams and the electrodes are realised by means of spring-damping elements (sdes). Fig. 8 shows the connection of strip j of electrode k with rfe e

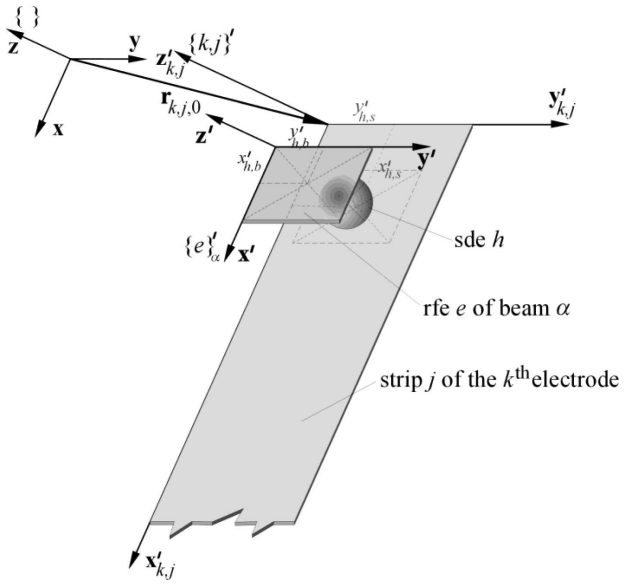

Fig. 8. Connection between strip j of electrode k and rfe e of beam α

of beam $\alpha(\alpha = u$ when the electrode is connected with the upper beam and $\alpha = d$ for the bottom beam). In the real structure of a system of electrodes, the axes of connections are usually parallel to the axes of global reference system {}.

Having taken into account the connections, we can write the equations of motion of the whole system which, regardless of the model of the electrodes used, take the form:

$$\underbrace{\begin{bmatrix} \mathbf{M}^{(u)} & 0 & \cdots & 0 & \cdots & 0 & 0 \\ 0 & \mathbf{M}^{(1)} & \cdots & 0 & \cdots & 0 & 0 \\ \vdots & \vdots & \ddots & \vdots & \vdots & \vdots & \vdots \\ 0 & 0 & \cdots & \mathbf{M}^{(k)} & \cdots & 0 & 0 \\ \vdots & \vdots & \vdots & \vdots & \ddots & \vdots & \vdots \\ 0 & 0 & \cdots & 0 & \cdots & \mathbf{M}^{(p)} & 0 \\ 0 & 0 & \cdots & 0 & \cdots & 0 & \mathbf{M}^{(d)} \end{bmatrix}}_{\mathbf{M}} \underbrace{\begin{bmatrix} \ddot{\mathbf{q}}^{(u)} \\ \ddot{\mathbf{q}}^{(1)} \\ \vdots \\ \ddot{\mathbf{q}}^{(k)} \\ \vdots \\ \ddot{\mathbf{q}}^{(p)} \\ \ddot{\mathbf{q}}^{(d)} \end{bmatrix}}_{\ddot{\mathbf{q}}} +$$

$$+ \underbrace{\begin{bmatrix} \mathbf{C}^{(u)} & \mathbf{C}_1^{(u)} & \cdots & \mathbf{C}_k^{(u)} & \cdots & \mathbf{C}_p^{(u)} & 0 \\ \mathbf{C}_u^{(1)} & \mathbf{C}^{(1)} & \cdots & 0 & \cdots & 0 & \mathbf{C}_d^{(1)} \\ \vdots & \vdots & \ddots & \vdots & \vdots & \vdots & \vdots \\ \mathbf{C}_u^{(k)} & 0 & \cdots & \mathbf{C}^{(k)} & \cdots & 0 & \mathbf{C}_d^{(k)} \\ \vdots & \vdots & \vdots & \vdots & \ddots & \vdots & \vdots \\ \mathbf{C}_u^{(p)} & 0 & \cdots & 0 & \cdots & \mathbf{C}^{(p)} & \mathbf{C}_d^{(p)} \\ 0 & \mathbf{C}_1^{(d)} & \cdots & \mathbf{C}_k^{(d)} & \cdots & \mathbf{C}_p^{(d)} & \mathbf{C}^{(d)} \end{bmatrix}}_{\mathbf{C}} \underbrace{\begin{bmatrix} \mathbf{q}^{(u)} \\ \mathbf{q}^{(1)} \\ \vdots \\ \mathbf{q}^{(k)} \\ \vdots \\ \mathbf{q}^{(p)} \\ \mathbf{q}^{(d)} \end{bmatrix}}_{\mathbf{q}} = \underbrace{\begin{bmatrix} -\mathbf{G}^{(u)} \\ -\mathbf{G}^{(1)} \\ \vdots \\ -\mathbf{G}^{(k)} \\ \vdots \\ -\mathbf{G}^{(p)} \\ -\mathbf{G}^{(d)} + \mathbf{Q}^{(d)} \end{bmatrix}}_{\mathbf{f}}. \tag{18}$$

The equations of motion were integrated by the Newmark method with a constant integration step which was chosen during some test calculations. Sets of algebraic linear equations were solved using Super LU library v.4.0 (2009), taking band matrices **M** and **C** into consideration.

3. Comparison of the models and their validation

Computer programmes in Delphi 7.0 were developed on the basis of the models presented. Vibrations of the system analysed can be simulated for different geometrical and mass parameters, for example different number, length and thickness of the electrodes or different number of strips in the

electrode. Different dimensions of the beams and different courses of the impulse force can be also analysed. Separately, the model in Abaqus was also formulated.

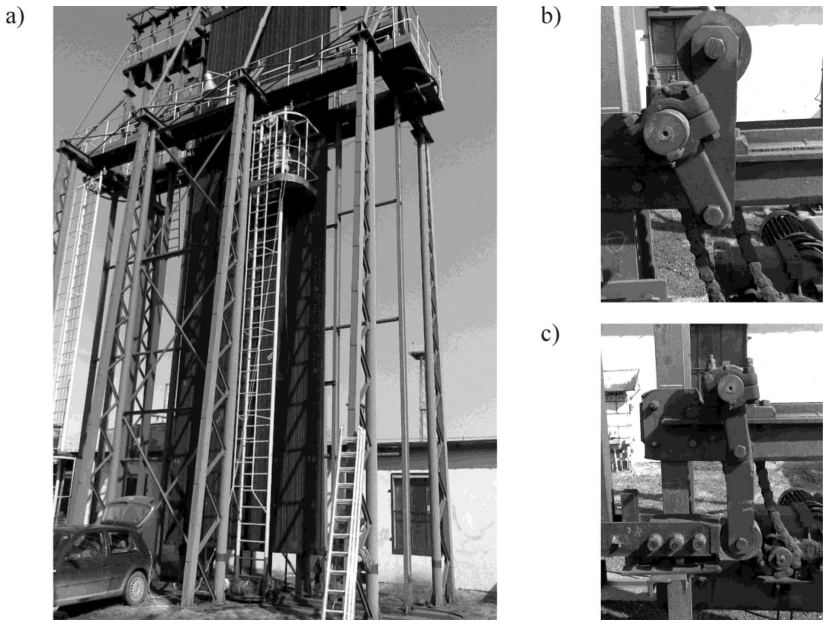

Fig. 9. Test stand: a) general view, b) initial and c) final position of the beater

The results of calculations for the system of electrodes were compared with those measured on the test stand (Fig. 9a). The impulse force is presented in Fig. 2c. The test stand contains nine SIGMA VI collecting electrodes with a length of 16.152 meters made of steel metal plates with a thickness of 0.0015 m.

In order to eliminate vibrations resulting from other sources than the beater, its drive was switched off. The motion of the beater started by releasing the beater from the position shown in Fig. 9b and finished by hitting the anvil (Fig. 9c). The measurements were carried out in calm conditions, in the temperature of about 20 degrees centigrade, using the apparatus consisting of: three–axial vibration sensors ICP 356A02 made by PCB Piezotronics, recorder TEAC LX110 and a laptop with LX Navi software. The signals were registered with a frequency of 24 kHz for each channel. The sensors were glued to the surface of the collecting electrodes. The scheme of position of the measurement points is presented in Fig. 10.

Vibrations of the electrodes are fast alternating processes and the direct comparison of courses is not effective. Thus in this paper we compare quantities representing indirectly the acceleration courses in the domain of

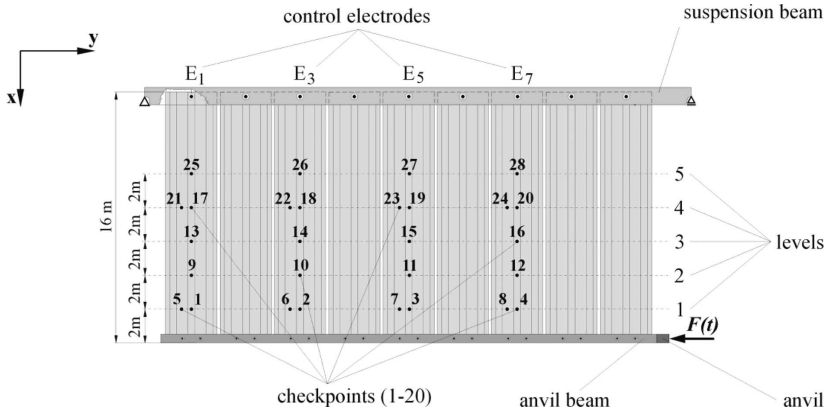

Fig. 10. Configuration of the control points in the system

amplitudes such as: peak value W_{Max}, maximal peak-to-peak value W_{PtP} and RMS value W_{RMS} defined by the following formulae:

$$W_{Max}\left(a_{s,\hat{s},i}\right) = \max_{o\le t\le T}\left|a_{s,\hat{s},i}\right|, \tag{19.1}$$

$$W_{PtP}\left(a_{s,\hat{s},i}\right) = \max_{o\le t\le T} a_{s,\hat{s},i}(t) - \min a_{s,\hat{s},i}(t), \tag{19.2}$$

$$W_{RMS}\left(a_{s,\hat{s},i}\right) = \left[\frac{1}{T}\int_0^T a^2_{s,\hat{s},i}\,dt\right]^{\frac{1}{2}}, \tag{19.3}$$

where: T – time of analysis,

$\hat{s}$ – index adopting values: N – when the signal was calculated according to authors' model, A – when Abaqus was used, M – when the signal was measured,

i – number of the control point.

It is assumed that $a_{s,\hat{s},i}$ occurring in the above formulae can be one of the following quantities:

$$a_{s,\hat{s},i} = \begin{cases} a_{x,\hat{s},i} & \text{– acceleration in the direction of axis } \mathbf{x}, \\ a_{y,\hat{s},i} & \text{– acceleration in the direction of axis } \mathbf{y}, \\ a_{\tau,\hat{s},i} = \sqrt{a^2_{x,\hat{s},i} + a^2_{y,\hat{s},i}} & \text{– tangential acceleration in plane } \mathbf{xy}, \\ a_{\nu,\hat{s},i} = a_{z,\hat{s},i} & \text{– normal acceleration to plane } \mathbf{xy}, \\ a_{c,\hat{s},i} = \sqrt{a^2_{x,\hat{s},i} + a^2_{y,\hat{s},i} + a^2_{z,\hat{s},i}} & \text{– total acceleration,} \end{cases}$$

and s belongs to $\{x, y, \tau, \nu, c\}$.

The indicators used in fluid mechanics [19], [20] for estimation of micro-scale and numerical models are applied as error measures:
– Factor $FAC2_\gamma$:

$$FAC2_\gamma = \frac{1}{n_p}\sum_{i=1}^{n_p} N_i^f, \tag{20.1}$$

$$N_i^f = \begin{cases} 1 & \text{for} \quad \frac{1}{2} \le \dfrac{W_\gamma\left(a_{s,N,i}\right)}{W_\gamma\left(a_{s,M,i}\right)} \le 2 \\ 0 & \text{otherwise} \end{cases}, \tag{20.2}$$

where: $W_\gamma\left(a_{s,N,i}\right)$, $W_\gamma\left(a_{s,M,i}\right)$ – calculated according to (19),
$\gamma \in \{Max, PtP, RMS\}$,
n_p – number of control points;
– Hit rate $q_\gamma\left(a_s\right)$:

$$q_\gamma\left(a_s\right) = \frac{1}{n_p}\sum_{i=1}^{n_p} N_i^q, \tag{21.1}$$

$$N_i^q = \begin{cases} 1 & \text{for} \quad \frac{1}{2} \le \dfrac{\left|W_\gamma\left(a_{s,N,i}\right) - W_\gamma\left(a_{s,M,i}\right)\right|}{W_\gamma\left(a_{s,M,i}\right)} \le \varepsilon \\ 0 & \text{otherwise} \end{cases}, \tag{21.2}$$

where: ε – admissible error.

The results are acceptable if for value examined γ the indicators are as follows: $FAC2_\gamma\left(a_s\right) \ge 0.5$ [21] and $q_\gamma\left(a_s\right) > 0.66$ [20].

In the graphs presenting values of those indicators the following notation is used for the calculations:

F – according to the FEM model,
H – according to the HFEM model,
S – according to the FSM model,
A – Abaqus,
M – for experimental measurements.

The calculations based on authors' models were carried out for $n_1 \div n_9 = 400$ and the integration step 5×10^{-6}s. Time of analysis was 0.02s.

Fig. 11 presents the values of indicators $FAC2_{Max}\left(a_s\right)$ and $q_{Max}\left(a_s\right)$. The values of $FAC2_{Max}\left(a_s\right)$ show good compatibility between the models and the experimental measurements. For each acceleration component analysed, values for not more than two control points are outside the acceptable range. In the case of indicator $q_{Max}\left(a_s\right)$ the differences are between 0% and 29%.

Models F and S show very good compatibility in peak–to–peak values of the normal component. In the case of the tangent component 4%–7% of points are outside the range of admissible errors. Model S is characterised by

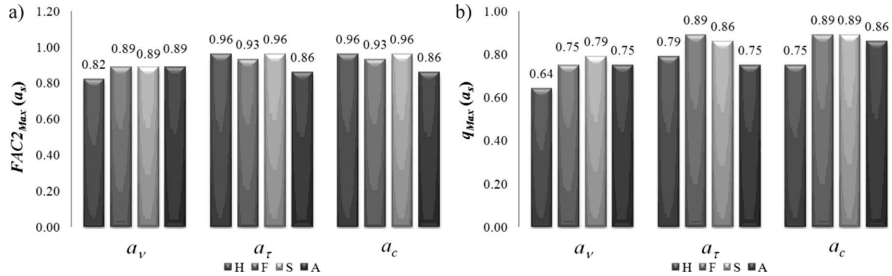

Fig. 11. Validation – indicators a) $FAC2_{Max}(a_s)$, b) $q_{Max}(a_s)$

a more uniform distribution of values of $q_{Max}(a_s)$. Only from 3 to 5 points are outside the admissible range.

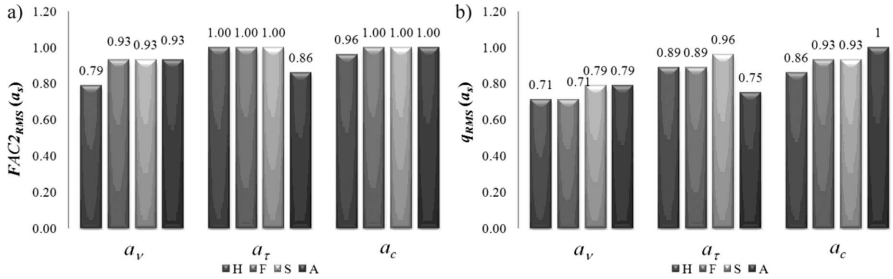

Fig. 12. Validation – indicators a) $FAC2_{RMS}(a_s)$, b) $q_{RMS}(a_s)$

The analysis of values of the indicators $FAC2_{RMS}(a_s)$ and $q_{RMS}(a_s)$ presented in Fig. 12 shows very good compatibility between the results obtained from models F and S and those of experimental measurements in the range of peak values of normal and tangent accelerations. In the case of model H the differences are observed at 3 to 5 control points for peak values of normal acceleration.

4. Final remarks

The models presented in the paper (FEM, HFEM, and FSM) differ considerably from each other in:

– functions approximating displacements u, v, w,
– ways of defining generalised coordinates,
– structure of mass **M** and stiffness **C** matrices.

This is the reason for the differences, and we can consider them justified and acceptable. It should be underlined that for the same time of analysis, integration step and number n_k (Table 1), calculation times are similar (Table 2). However, numbers of non–zero elements in matrices **M** and **C** are different. For that reason it is difficult to state which method is better,

Table 1.

Numerical parameters of models

Simulation time	$T = 2 \times 10^{-2} s$
Integration step	$h_c = 5 \times 10^{-6} s$
Number of elements in a strip	$n_k = 400$

either in terms of numerical effectiveness or compatibility with experimental measurements.

Table 2.

Time of numerical simulation and numbers of generalised coordinates

Model	**A**	**M**	**H**	**S**
Step a: Generation of matrices **M** and **C**	–	21 s	18 s	297 s
Step b: Calculation of initial conditions, solution of statics	–	97 s	79 s	131 s
Step c: Integration of equations of motion	–	8302 s	2808 s	10545 s
Total time of realisation of algorithms a-c	169000 s	8420 s	2905 s	10973 s
Number of generalised coordinates	–	433698	498660	290778

The validation of results presented in the paper proves that all models correctly reflect the dynamics of the rapping system in the range of accelerations of vibrations induced by an impulse force.

Manuscript received by Editorial Board, December 3, 2012;
final version, March 12, 2013.

REFERENCES

[1] Pope III C.A., Burnett R.T., Thun M.J., Calle E.E., Krewski D., Ito K., Thurston G.D.: Lung Cancer, Cardiopulmonary Mortality and Long-Term Exposure to Fine Particulate Air Pollution, JAMA 287(9) (2002) 1132-1141.
[2] Filleul L., Rondeau V., Vandentorren S., Le Moua N., Cantagrel A., Annesi-Maesano I., Charpin D., Declercq C., Neukirch F., Paris C., Vervloet D., Brochard P., Tessier J.F., Kauffmann F., Baldi I.: Twenty five year mortality and air pollution: results from the French PAARC Survey, Occup. Environ. Med. 62 (2005) 453-460.
[3] Woodruff T.J., Parker J.D., Schoendorf K.C.: Fine Particulate Matter (PM2.5) Air Pollution and Selected Causes of Postneonatal Infant Mortality in California, Environ. Health Perspect. 114(5) (2006) 786-790.
[4] Meroth A.M., Gerber T., Munz C.D., Schwab A.J.: A model of the non-stationary charge flow in an electrostatic precipitator, Proceedings: ICESP VI, (1996), Hungary.
[5] Strehlow A., Schmoch M.: Comparison of Techniques for Electrode Rapping in Electrostatic Precipitators, Proceedings: ICESP VIII, (2001), USA.
[6] Long Z., Yao Q., Song Q., Li S.: A second-order accurate finite volume method for the computation of electrical conditions inside a wire-plate electrostatic precipitator on unstructured meshes, Journal of Electrostatics 67(4) (2009) 597-604.

[7] Neimarlija N., Demirdžić I., Muzaferij S.: Finite volume method for calculation of electrostatic fields in electrostatic precipitators, Journal of Electrostatics 67(1) (2009) 37-47.
[8] Sarna M.: Influence of dust Re-entrainment and skew gas-flow technology on ESP efficiency, Proceedings: ICESP VIII Conference, May 14-17, 2001, Birmingham, Alabama, USA, 2001.
[9] Kim S.H., Lee K.W.: Influence of Contaminated Discharging Electrode and Collection Plates on Particle Collection Characteristics of ESP, Proceedings: ICESP VII, (1998), Korea.
[10] Nowak A., Wojciech S.: Optimisation and experimental verification of a dust-removal beater for the electrodes of electrostatic precipitators, Computers and Structures 82(22) (2004) 1785-1792.
[11] Nowak A.: Modelling and measurements of vibrations of collecting electrodes in dry electrostatic precipitators, Monograph (habilitation), Bielsko-Biała University Press, Poland, 2011 (in Polish).
[12] Nowak A.: Numerical verification and experimental validation of the FEM model of collecting electrodes of dry electrostatic precipitators, Latin American Journal of Solids and Structures (in print) (2012).
[13] Adamiec-Wójcik I.: Modelling of Systems of Collecting Electrodes of Electrostatic Precipitators by means of the Rigid Finite Element Method, The Archive of Machanical Engineering LVIII(1) (2011) 27-47.
[14] Adamiec-Wójcik I., Nowak A., Wojciech S., Application of the finite strip method to modelling of vibrations of collecting electrodes, International Journal of Structural Stability and Dynamics (in print) (2012).
[15] Adamiec-Wójcik I., Nowak A., Wojciech S.: Comparison of methods for vibration analysis of electrostatic precipitators, Acta Mechanica Sinica 1 (2011) 72-79.
[16] Wittbrodt E., Adamiec-Wójcik I., Wojciech S.: Dynamics of flexible multibody systems Rigid finite element method, Springer-Verlag, Berlin Heidelberg, 2006.
[17] Huang M., Zhao Z., Shen C.: An effective planar triangular element with drilling rotation, Finite Elements in Analysis and Design 46 (2010) 1031-1036.
[18] Zienkiewicz O.C., Taylor R.L.: The finite element method Vol.2: Solid Mechanics, Bulterworh-Heinemann, 2003.
[19] Britter R., Schatzmann M. (ed): Background and justification document to support the model evaluation guidance and protocol, COST Action 732, COST Office, Brussels, 2007.
[20] VDI Guideline on environmental meteorology – prognostic microscale wind field models – evaluation for flow around buildings and obstacles, 3783 part 9, Dusseldorf, 2005.
[21] Chang J.C., Hanna S.R.: Technical Descriptions and User's Guide for the BOOT Statistical Model Evaluation Software Package, Version 2.0., 2005.

Porównanie metod modelowania drgań elektrod osadczych elektrofiltru suchego

Streszczenie

Elektrofiltry suche są powszechnie stosowane do odpylania przemysłowych gazów spalinowych. Utrzymanie ich wysokiej skuteczności zależy przede wszystkim od okresowego oczyszczania elektrod osadczych. Usuwanie pyłu z ich powierzchni realizuje się poprzez wywołanie okresowych drgań elektrod. W pracy przedstawiono wyniki modelowania drgań układu elektrod osadczych. Wyniki uzyskano za pomocą metod: metody elementów skończonych, hybrydowej metody elementów skończonych, metody pasm płytowych oraz modelu sformułowanego w pakiecie ABAQUS. Wyniki obliczeń numerycznych porównano z wynikami uzyskanymi z pomiarów doświadczalnych. Sformułowano wnioski dotyczące skuteczności i numerycznej dokładności modeli oraz przedyskutowano przyczyny różnic występujących pomiędzy nimi.